Hindawi
Advances in Civil Engineering
Volume 2020, Article ID 8841796, 21 pages
https://doi.org/10.1155/2020/8841796

Research Article

Effect of Material Properties and Strain Rate on Fragmentation of Anisotropic Rock

R. J. Wu [1,2] and H. B. Li [1,2]

[1] *State Key Laboratory of Geomechanics and Geotechnical Engineering, Institute of Rock and Soil Mechanics, Chinese Academy of Sciences, Wuhan 430071, China*
[2] *University of Chinese Academy of Sciences, Beijing 100049, China*

Correspondence should be addressed to H. B. Li; hbli@whrsm.ac.cn

Received 6 July 2020; Revised 6 September 2020; Accepted 21 September 2020; Published 13 October 2020

Academic Editor: Fengqiang Gong

In order to investigate the effect of the microproperties of bedding and strain rate on the fragment size distributions of layered phyllite with different bedding dip angles, a split Hopkinson pressure numerical model was established and verified by comparing with the experimental results. A new method to obtain reasonable layered rock dynamic simulation result was proposed. Then, the cumulative distribution curve and average fragment size of layered rocks were calculated after changing the strain rate and microparameters of bedding in the model. The results showed that the samples tend to become pulverized under high strain rate, and it was harder for the samples with low dip angle to be damaged if the bedding shear strength is added, while the fragmentation of high angle samples did not change significantly. Furthermore, the failure of layered specimens was not affected by the tensile strength and stiffness. The wider bedding and narrower space promoted the crack initiation and propagation.

1. Introduction

Rock splintering under high rate load could be observed in blasting [1], tunneling [2], earthquakes [3], rock bursts, and shale gas well fracturing [4, 5]. Therefore, it is essential to investigate the rock fragmentation behavior for solving many practical engineering problems, such as blasting and excavation could be achieved more safely and economically, efficient rock disintegration, and reliable architectural design [6–8].

During a brittle fragmentation event, microcracks originate under stress concentrations, open, propagate rapidly to interact with another, and eventually coalesce to form separated fragments. Due to the complexity of dynamic rock fracture, a range of experiments, theoretical models, and computational simulations have been pursued to enrich the knowledge of the fragmentation over the past several decades [9–12]. Rosin and Rammler [9] constructed a fragment size distributions function, which is quoted to form the widely used blasting prediction fragmentation model [1]. Besides a series of theoretical analysis [10, 11], a variety of simulation methods have been done to provide insights into the rock pulverization process. Zhou and Molinari [12] used a finite element ring model to study the dynamic fragmentation properties of materials under tensile impact load. The effects of ring size, the energy conversions, and related properties are discussed. With the help of the grain-based discrete element method (GB-DEM), Li et al. [13] put forward that there exist two classes of broken behavior corresponding to the different rock pulverization phenomenon under dynamic loads.

Recent investigations have reported that the debris size is determined by initial defect properties [14], and thus more attention has been paid to the effect of heterogeneity on rock fragmentation. Levy and Molinari [15] extended the work of Zhou and Molinari [12] by including defect distributions to analyze the influence of defects on average fragment size. The results showed that the distribution tail has a critical influence on the fragmentation process. Paliwal and Ramesh [16] concluded that the spread of the preexisting flaw

distribution is critical at low rates, while the flaw density is crucial under high strain rate load. The rock appears transversely isotropic as the microstructural defects are arranged in a preferred orientation, which means the bedding plane dominates the fragment size distributions. However, on the one hand, defects and fragmentation remain an open issue [16]; especially the effect of rock heterogeneity on fragment is not clear. On the other hand, although there are some reports on the mechanical properties of layered rocks [17, 18], few studies have involved how the bedding properties affect rock fragmentation.

The discrete element model not only could simulate the initiation, growth, and coalescence of microcracks during rock failure, but also directly reproduce the fragmentation of the rock [18–20]. Defects in rock such as bedding could also be simulated [21]. Three-dimensional discrete element model has obtained fragment with high fidelity [19]. Nonetheless, 3D simulations of rock fragmenting structures show technical limitations related to the computational cost when analyzing an extensive amount of data. The 2D numerical model could be utilized to observe a number of phenomena, for example, fragmentation, spallation, and damage evolution [22, 23]. Considering that numerous model calculations are needed in the study of layered rocks, the 2D model approach offers an efficient compromise between accuracy and complexity. Therefore, 2D discrete element model is selected to explore the effect of different parameters on the layered rock fragmentation.

In this study, quasistatic and dynamic tests for layered phyllite with different bedding dip angle were done to calibrate the microscopic parameters of the two-dimensional discrete element model. Experimental and numerical stress-time curves and ultimate fragment states were compared to validate the model. Then the parameters of the bedding plane and the strain rate were changed to investigate the dynamic fragmentation. The numerical results were analyzed to determine how the microscopic properties of bedding plane and strain rate affect the fragment size distributions of layered rock with different bedding dip angle.

2. Specimen Preparation and Experimental Setup

2.1. Specimen Preparation. Since there is no well theoretical method to define the parameters of the discrete element model through the macroparameters of rock and also to provide reference for the verification of the model, the layered phyllite is selected as the sample of dynamic experiment. The X-ray analysis indicates that the sample is mainly composed of three kinds of mineral: muscovite (28.94%), chlorite (20.82%), and albite (19.47%), respectively. The rest of the minerals are quartz (19.16%), calcite (9.55%), and others (2.06%). The typical layered structure has been inspected by a scanning electron microscope (SEM), as shown in Figure 1. According to the International Society for Rock Mechanics (ISRM) suggestion [24], the diameter and height of samples are 50 mm and 25 mm, respectively. All 30 samples are divided equally into quasistatic and dynamic group, which are cut from a block, as shown in Figure 2(a). Five bedding dip angles (0°, 22.5°, 45°, 67.5°, and 90°) are included in each group, and the definition of bedding dip angle β is presented in Figure 2(b).

2.2. Split Hopkinson Pressure Bar (SHPB). The SHPB tests system, located at the State Key Laboratory of Wuhan Institute of geotechnical mechanics, is employed to obtain rock fragment. The apparatus comprises a striker (400 mm × Φ50 mm), an incident bar (2500 mm × Φ50 mm), a transmitted bar (2500 mm × Φ50 mm), and an absorber (1000 mm × Φ50 mm), as shown in Figure 3. All these components are constructed by alloy steel with elastic modulus of 210 GPa, P-wave velocity 5189 m/s, and density of 7800 kg/m^3. The layered phyllite is placed between the incident bar and the transmitted bar. In order to satisfy the assumptions of stress equilibrium in the sample and stress wave propagation in one dimension [25, 26], a bullet-shape striker and pulse shaper are used to provide a smooth incident wave stress [27]. The incident strain wave $\varepsilon_I(t)$, the reflected strain wave $\varepsilon_R(t)$, and the transmitted strain wave $\varepsilon_T(t)$ are recorded by the dynamic strain gauges mounted on the incident bar and transmitted bar to calculate the strain rate $\dot{\varepsilon}(t)$, strain $\varepsilon(t)$, and stress $\sigma(t)$[28]:

$$\left.\begin{aligned} \dot{\varepsilon}(t) &= \frac{c}{l_0}\left(\varepsilon_I - \varepsilon_R - \varepsilon_T\right) \\ \varepsilon(t) &= \frac{c}{l_0}\int_0^t \left(\varepsilon_I - \varepsilon_R - \varepsilon_T\right)dt \\ \sigma(t) &= \frac{A}{2A_0}E\left(\varepsilon_I + \varepsilon_R + \varepsilon_T\right) \end{aligned}\right\}, \quad (1)$$

where c is the P-wave velocity of the bar material, l_0 is the length of the specimen, E is the Young modulus of the bar material, and A and A_0 are the cross-sectional area of the bars and sample, respectively.

2.3. Experimental Results. The three-wave method should be done to judge whether the stress at both ends of the sample is the same to guarantee stress equilibrium during the application of impact load [29]. Figure 4 shows the dynamic stress at the incident and the transmission bar ends of samples. The agreement between σ_t and $\sigma_i + \sigma_r$ indicates that stress equilibrium is achieved.

Quasistatic tests of layered phyllite were carried out on the rock mechanics experimental (RMT) device. The quasistatic and dynamic mechanical properties of layered phyllite are listed in Table 1, which would be utilized to calibrate parameters of numerical model.

3. Numerical Model in DEM

3.1. Model Setup. The bonded-particle model (BPM) [30] is performed to build the SHPB numerical simulation test system. The SHPB bars and rock matrix are characterized by the parallel bond model and the smooth joint model is inserted to solve the inherent roughness problems [31]. As

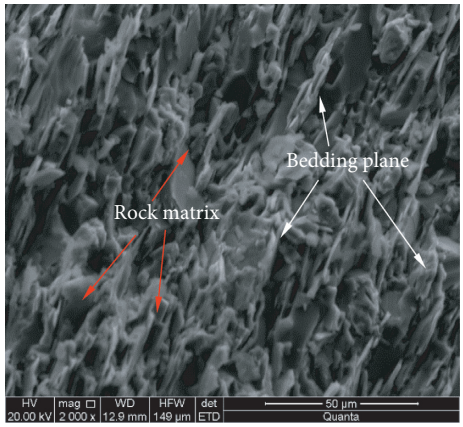

Figure 1: Layered structure observed under SEM.

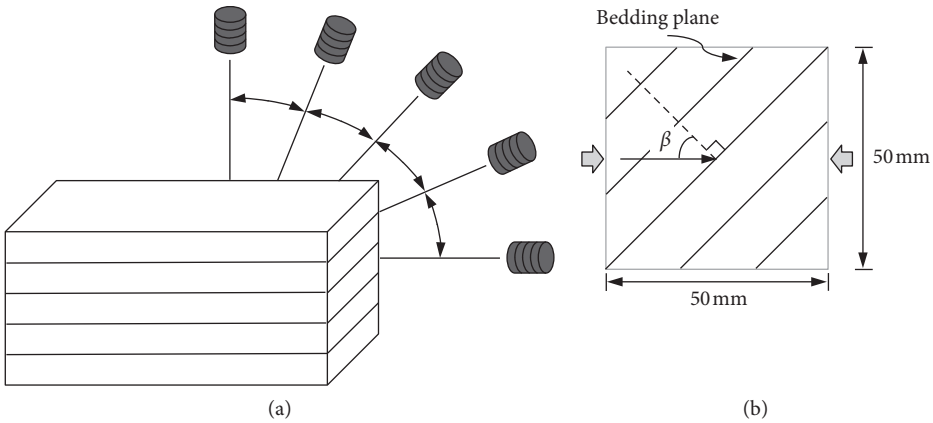

Figure 2: Preparation of layered phyllite specimens with different bedding angles. (a) Schematic diagram of sample acquisition. (b) Definition of bedding angle and specimen size.

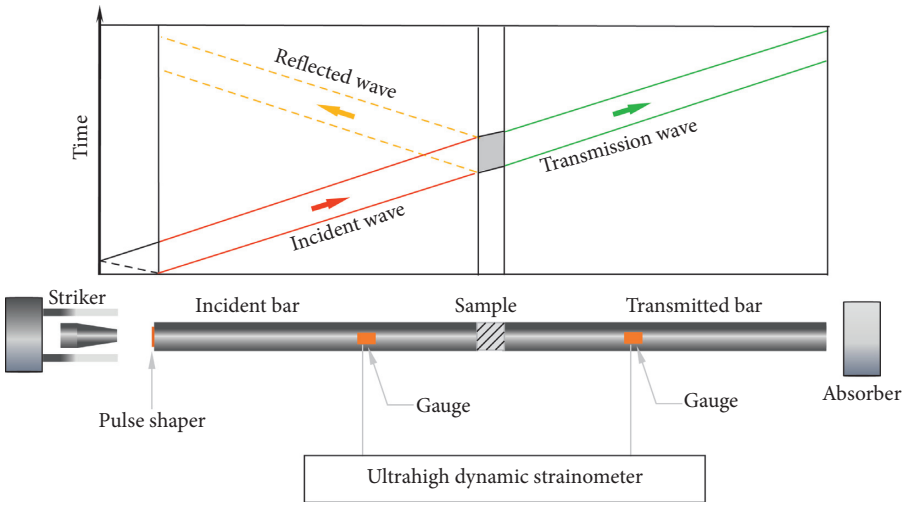

Figure 3: SHPB system and stress wave propagation situation.

illustrated in Figure 5, the incident bar and the transmitted bar are all set to 1500 mm, which is long enough to avoid superposition between the stress wave [20]. The microscopic properties of particles and bonds assigned to the SHPB bars are tabulated in Table 2. The Young modulus and density are consistent with the laboratory apparatus. Using regular-distributed particles to construct the SHPB simulation device model could only reproduce the homogeneous of alloy steel, but also effectively ensure the one-dimensional wave propagation [13]; thus, the regular distribution of 5 mm

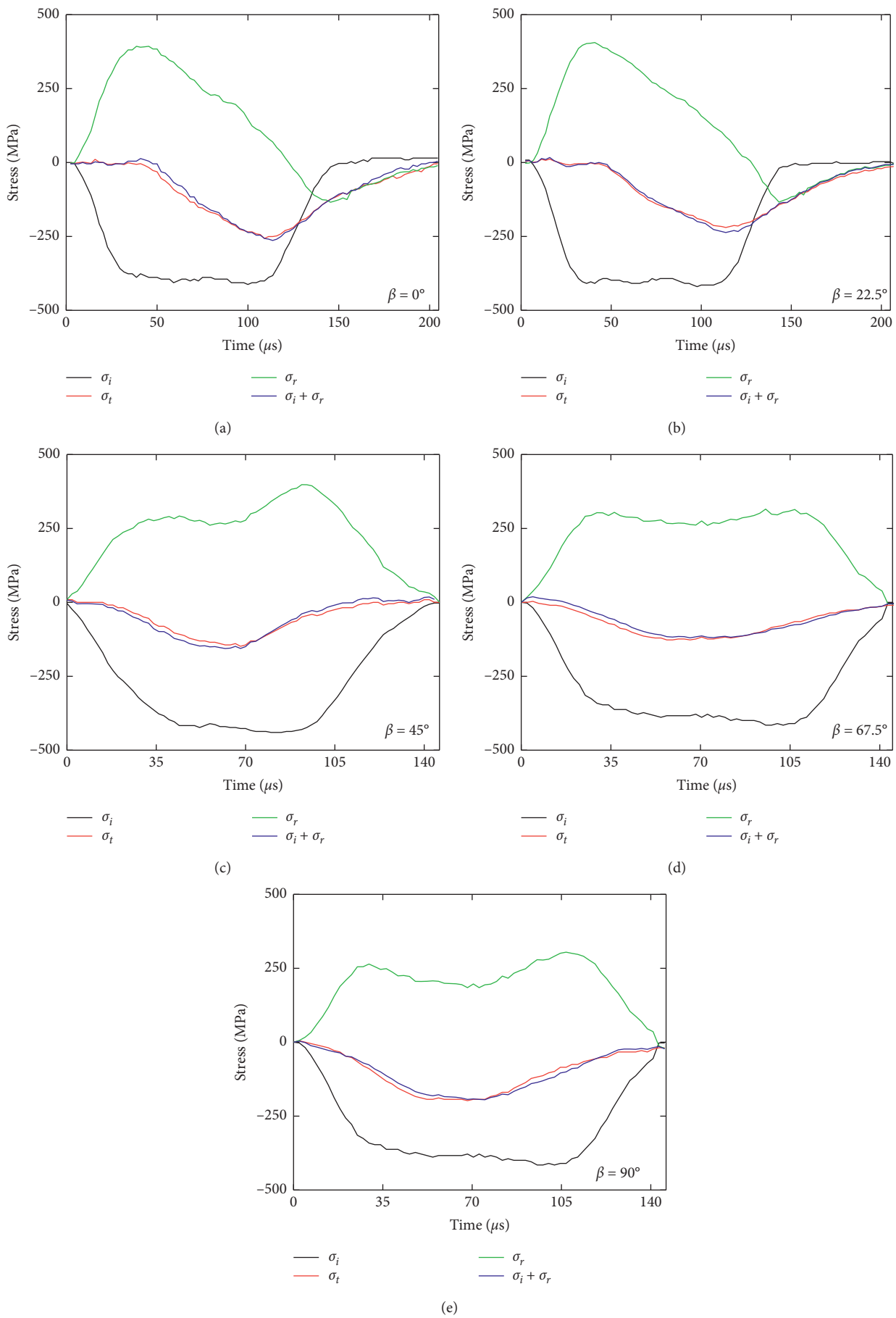

Figure 4: Three-wave method to check experimental stress equilibrium.

Table 1: Quasistatic and dynamic mechanical properties of layered phyllite.

Bedding angle β	0	22.5	45	67.5	90
Quasistatic elastic modulus (GPa)	17.1	29.1	25.6	27.7	19.4
Quasistatic compression strength (MPa)	152.2	127.7	73.6	63.1	115.7
Dynamic strain rate (s^{-1})	94.8	99.4	138.2	142.6	137.2
Dynamic compression strength (MPa)	248.1	214.6	143.2	122.5	187.0

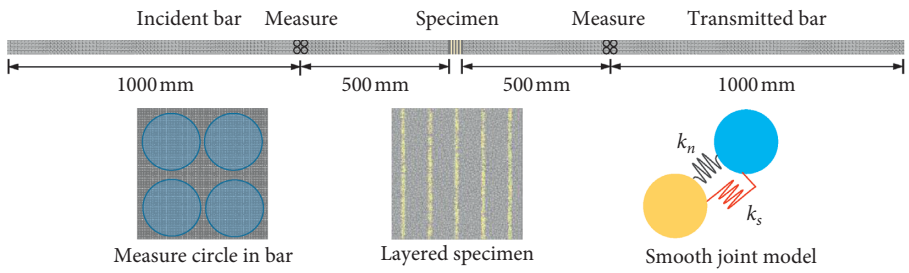

Figure 5: The SHPB numerical simulation test system.

Table 2: Microscopic properties of particles and bonds of the SHPB bars.

Properties	Material parameters' value
Particles	
Ball density (kg/m^3)	7900
Ball radius (m)	0.5e-3
Particle-based material parameters	
Young's modulus (E_c, Pa)	182e9
Stiffness ratio (k_n/k_s)	2.35
Parallel bond model parameters	
Young's modulus ($\overline{E}_c$, Pa)	182e9
Stiffness ratio ($\overline{k}_n/\overline{k}_s$)	2.35
Normal strength (σ_c, Pa)	1e100
Shear strength (τ_c, Pa)	1e100

particles is employed to form the bar model. The tensile strength and shear strength of the SHPB bars are both set as 1e100 Pa to ensure that they would not be damaged during wave propagation.

Calibration for sample parameters is cautious to accomplish several steps to reproduce the real experimental process. The 0° sample and 90° sample under quasistatic load are employed to preliminary determine the strength and Young's modulus of numerical model, respectively. The 67.5° sample is selected to identify the smooth joint bond strength considering the layered rock with this angle failed along the bedding planes. Then, the stiffness of the bedding are obtained by using the equivalent continuous model [22]. Before completing the model, dynamic test results are utilized to correct the parameters. The microscopic properties of particles and bonds of the sample are listed in Table 3.

3.2. Validation of the DEM Model

3.2.1. Dynamic Stress Equilibrium. A successful SHPB experiment must meet two requirements: the stress wave propagates in the form of one-dimensional wave in the bar, and the dynamic stress at both ends of the specimen remains equal during the loading process. Li et al. [20] have proved that homogeneous particles could well maintain the one-dimensional propagation of stress waves in the DEM model. The three-wave method, as an indirect approach, is employed to compare the force of the specimen on two ends in laboratory experiments, after considering that the axial force of the specimen is hard to measure directly [26]. However, the forces at both ends of specimen could be directly obtained to judge whether it is in a stress equilibrium state in the numerical model. Therefore, the three-wave method and the direct measurement method are both applied to guarantee that the sample be in the dynamic stress equilibrium state during the impact loading process. The result of the three-wave method is presented in Figure 6(a), which demonstrates that forces at both ends of the specimen calculated by the incident bar and the transmission bar are basically equal.

For the direct measurement method, stress on the left and right end of the sample is directly recorded. The stress equilibrium coefficient $\eta = 2(\sigma_{\text{right}} - \sigma_{\text{left}})/(\sigma_{\text{right}} + \sigma_{\text{left}})$ is calculated to compare the stresses at both ends of the sample. As shown in Figure 6(b), η remains around zero near the peak sections, which directly indicates that the axial force of the specimen is equal during the loading process.

3.2.2. Ultimate Fragment States. To further validate the BPM numerical model, dynamic tests on the 45° samples are simulated. The incident stress wave of 45° sample is derived from the experiment to ensure the numerical dynamic stress is comparable with the experimental, as shown in Figure 7(a). Figures 7(b)~7(f) illustrate the experimental and numerical dynamic uniaxial compression stress–time curve for five angle samples, whose values and change trends are basically consistent. The dynamic compressive strength of layered rock changes in U-shape with the increase of bedding angle, and the strength is the minimum at 67.5°. Figure 7(g) depicts ultimate fragment state of five angle

Table 3: Microscopic properties of particles and bonds of the sample.

Properties	Material parameters' value
Particles	
Ball density (kg/m^3)	2620
Minimum ball radius (m)	$0.2e-3$
Maximum ball radius (m)	$0.332e-3$
Young's modulus (E_c, Pa)	$16.4e9$
Stiffness ratio (k_n/k_s)	1.15
Parallel bond model	
Young's modulus ($\overline{E}_c$, Pa)	$16.4e9$
Stiffness ratio (pb_k_n/pb_k_s)	1.15
Normal strength (pb_σ_c, Pa)	$52e6 \pm 13e6$
Shear strength (pb_τ_c, Pa)	$140e6 \pm 35e6$
Smooth joint model	
Normal stiffness (sj_k_n (Pa/m))	$15.73e12$
Shear stiffness (sj_k_s (Pa/m))	$6.38e12$
Friction coefficient (φ)	35°
Cohesion (sj_τ_c, Pa)	$36e6 \pm 3e6$
Tensile strength (sj_σ_c, Pa)	$3e6 \pm 0.5e6$

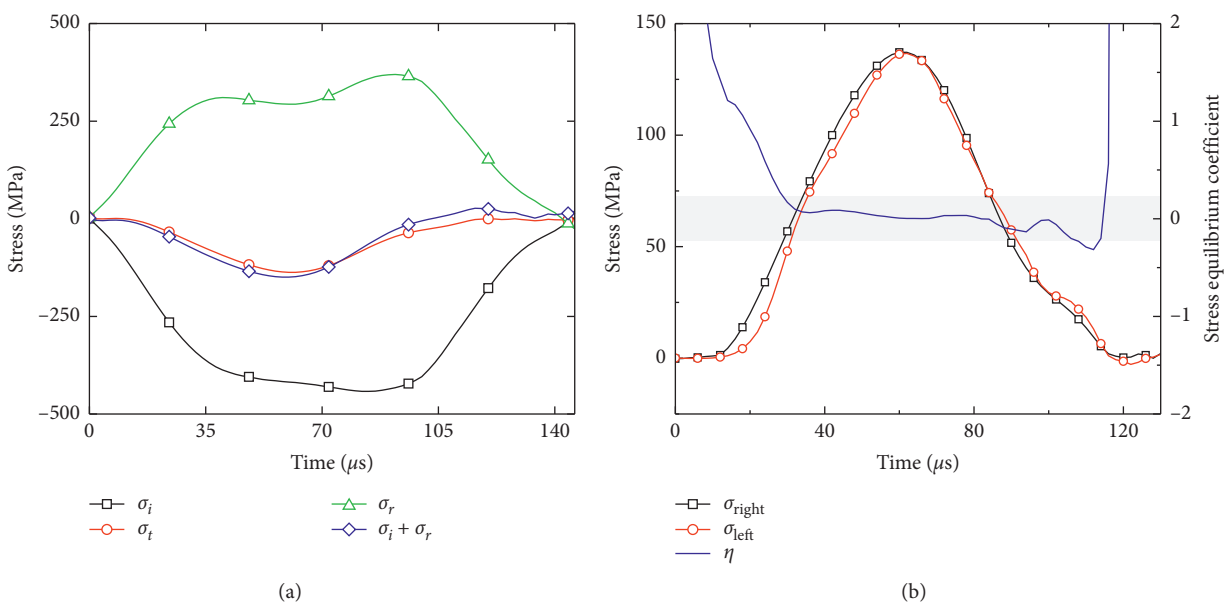

Figure 6: The dynamic stress equilibrium state of SHPB numerical model. (a) Three-wave method to check numerical stress equilibrium. (b) Direct measurement method to check stress equilibrium.

samples after the experimental and numerical tests at the strain rate ≈140 s^{-1}. The simulation results of low bedding angle samples show that the bedding plane affects the local failure of the samples. High bedding angle samples are broken into schistose along the bedding and partially pulverized in both situations. These results indicate that the SHPB numerical simulation test system is reasonable to characterize the realistic behaviors of layered phyllite.

4. Results and Discussion

The particles that are still bonded together after loading are defined as a fragment. The fragment that is composed by individual particle is not counted to simplify the calculation. The cumulative distribution curve of layered rocks with five bedding angles is counted in different situation. What is more, the average fragment size is calculated to quantitatively compare the damage:

$$\overline{\delta} = \frac{\sum_{i=1}^{n} \eta_i \delta_i}{\sum_{i=1}^{n} \eta_i}, \tag{2}$$

where n is the total fragment number, δ is the area of the ith fragment, and η represents the percentage of the ith fragment area.

4.1. Effect of Strain Rate. Five impact velocities were applied to the simulation layered samples to obtain the fragmentation under different strain rates. As shown in Figure 8, the loading strain rate has a significant effect on the strength and

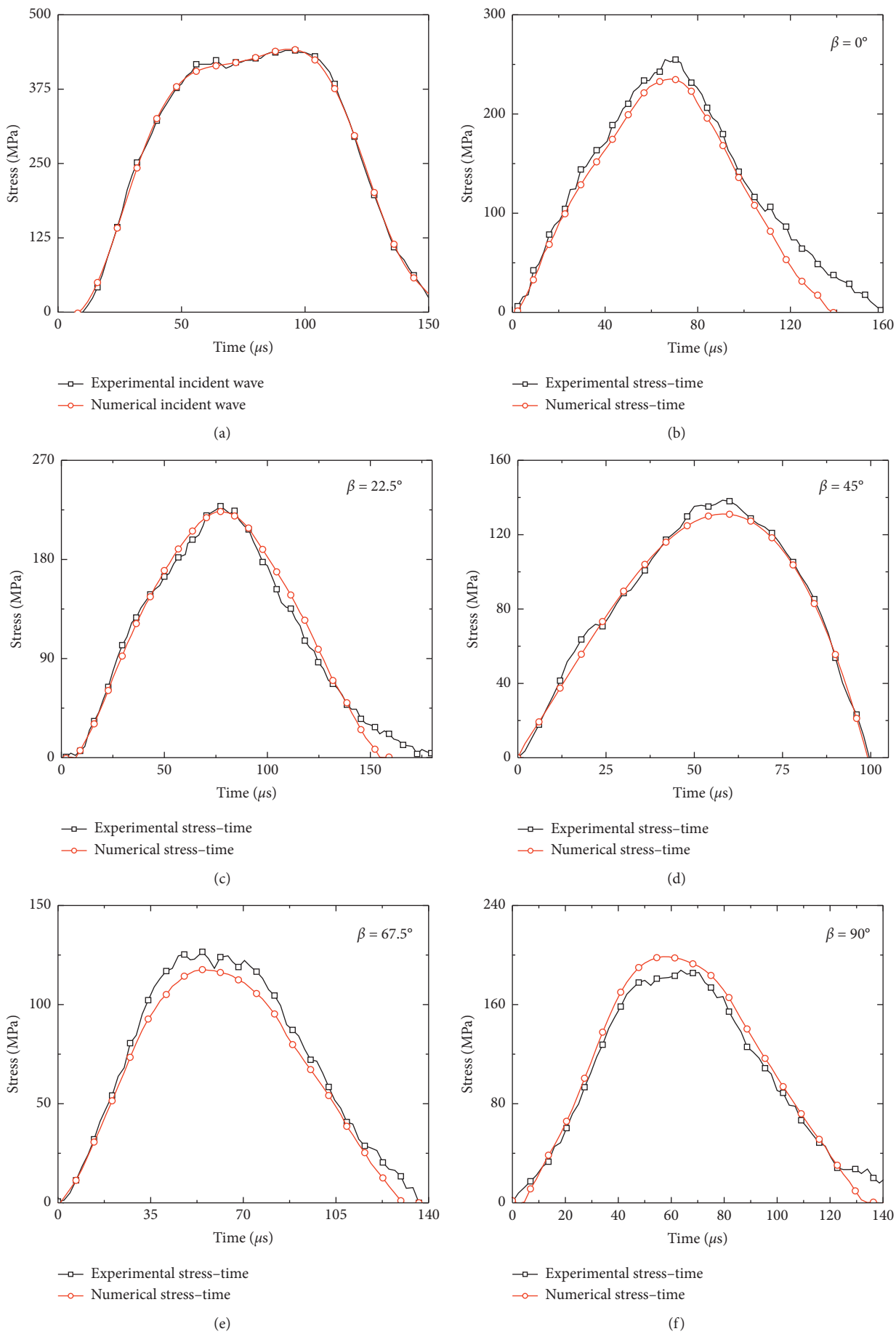

Figure 7: Continued.

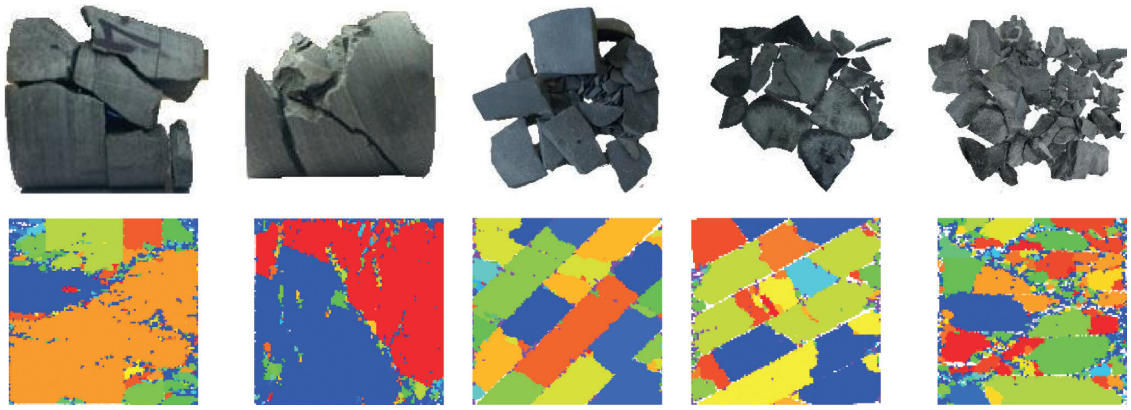

(g)

Figure 7: SHPB numerical model and simulation results. (a) Numerical and experimental incident stress wave of 45° sample. (b–f) Numerical and experimental dynamic compression stress of five angle samples. (g) The ultimate fragment state of five angle samples after experiment and simulation.

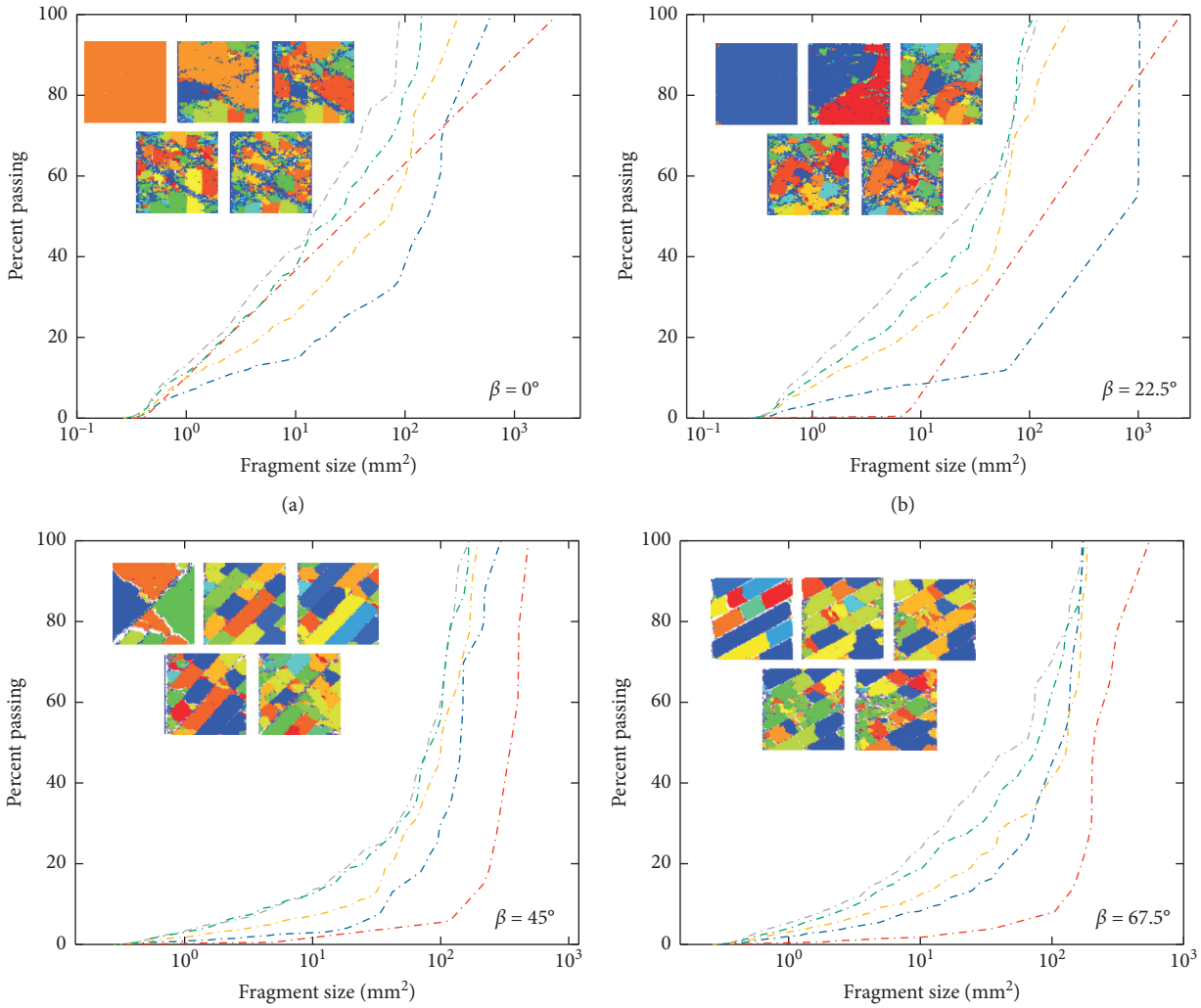

(a) (b) (c) (d)

Figure 8: Continued.

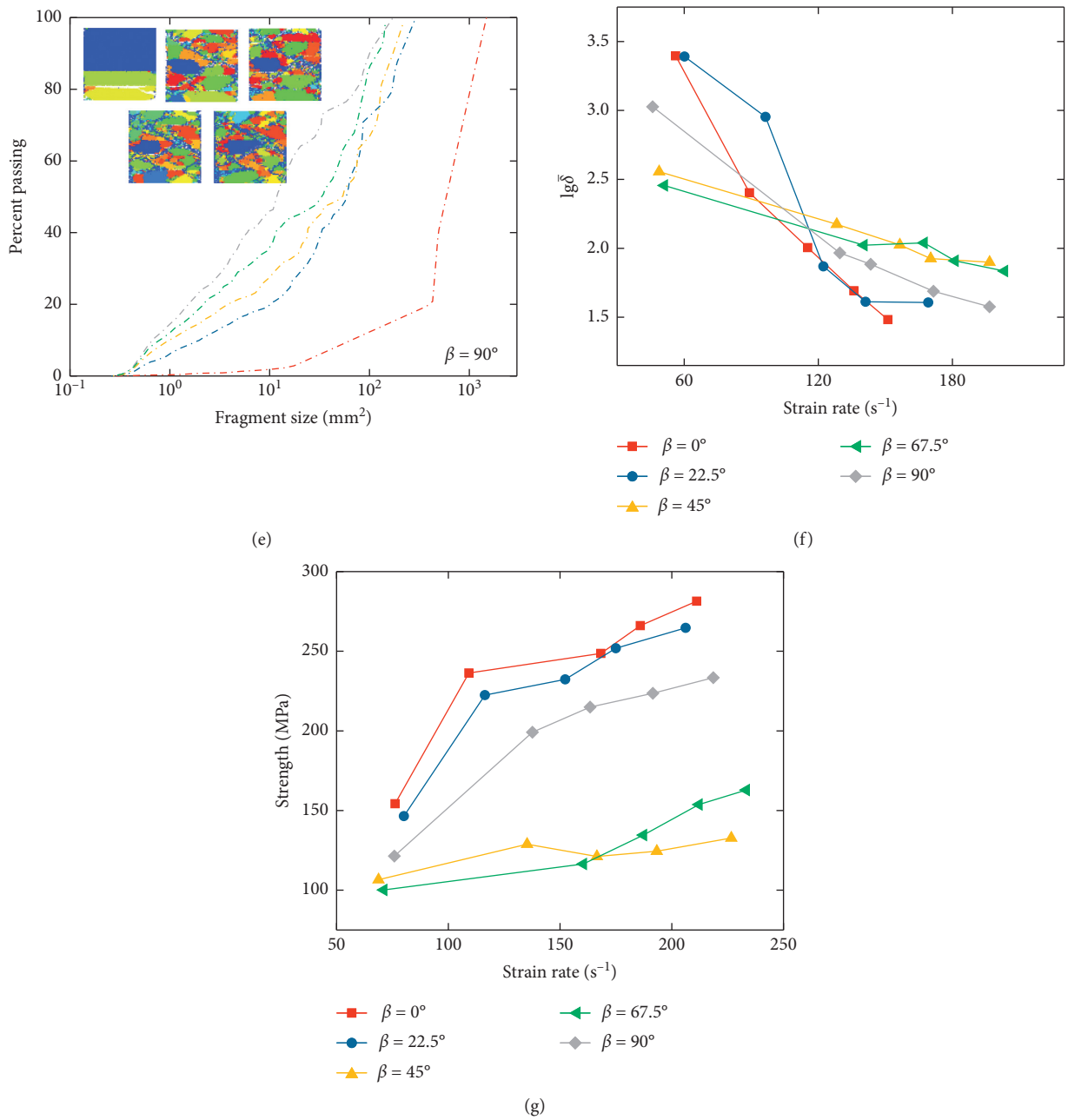

Figure 8: The cumulative distribution curve and average fragment size of layered rocks under different strain rates. (a–e) The distribution curve of 0°, 22.5°, 45°, 67.5°, and 90° samples, red: $\dot{\varepsilon} \approx 80\ s^{-1}$, blue: $\dot{\varepsilon} \approx 140\ s^{-1}$, yellow: $\dot{\varepsilon} \approx 170\ s^{-1}$, green: $\dot{\varepsilon} \approx 200\ s^{-1}$, and gray: $\dot{\varepsilon} \approx 215\ s^{-1}$. (f) Average fragment size vs. strain rate under different bedding angles. (g) Dynamic strength vs. strain rate under different bedding angles.

failure of the specimen. Under any dynamic load, the strength of the specimen always presents a U-shaped change with the increase of bedding angle, and the minimum strength occurs at 45°–67.5°.

The fragment size decreases gradually as the strain rate increases, while the strength presents an opposite trend. The samples with low bedding angle show minor damage under smaller impact load and that changes at higher strain rate. With the increase of strain rate, more cracks initiate along the loading direction and propagate to intersect with the cracks on the weak bedding plane of 0°–22.5° sample, which leads to further failure of the specimen.

Although the impact splitting effect is increased, the weak bedding plane limits the crack to the local part of 45°–67.5° specimen and hinders its further expansion, causing specimens' difficulty to be further destroyed. As shown in Figure 8, when reaching a certain strain rate, the shiver of rocks with $\beta = 45°–67.5°$ tends to be stable. The results explored that in order to achieve better fragmentation under high strain rate, the relationship between the loading

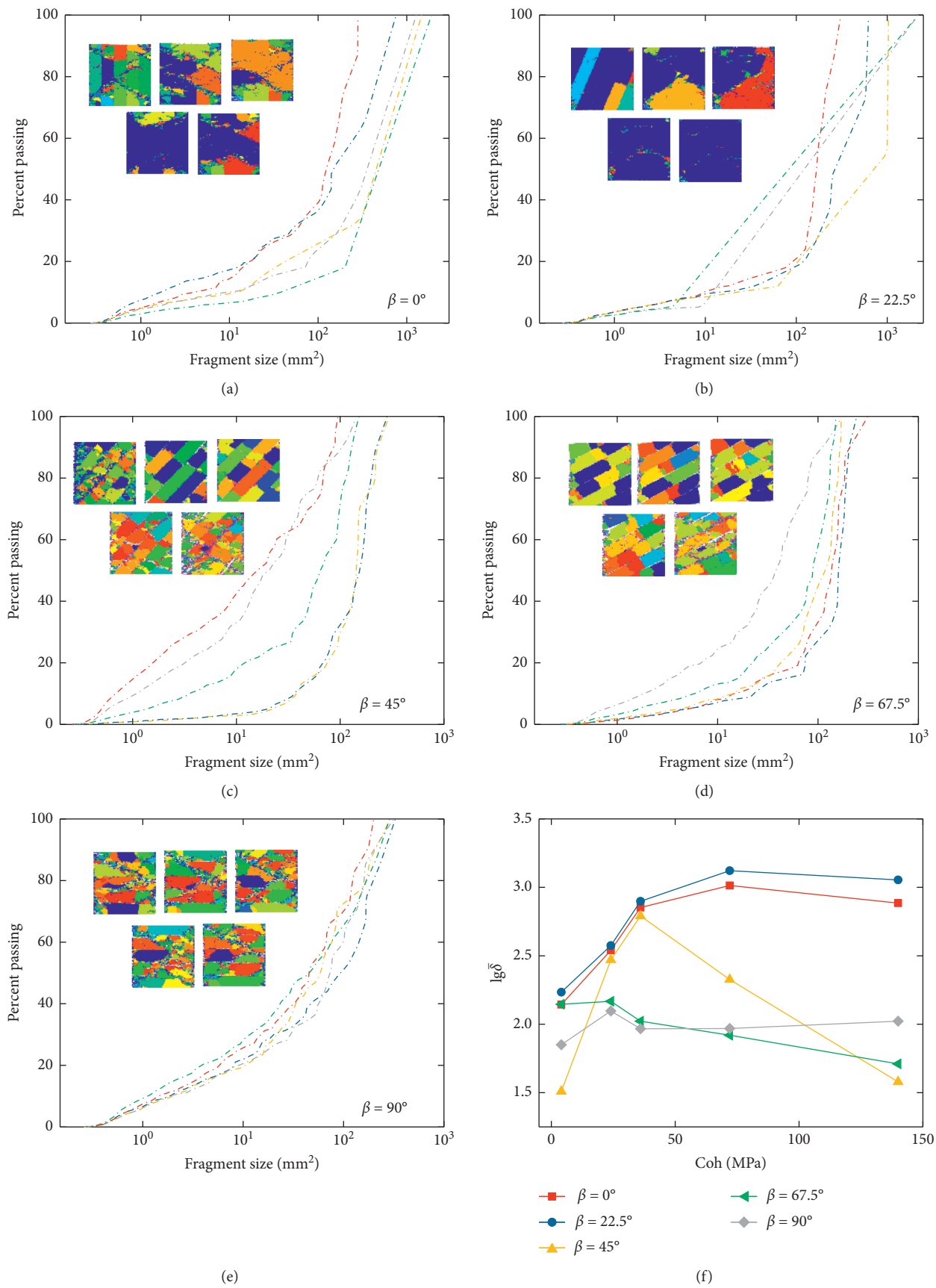

Figure 9: Continued.

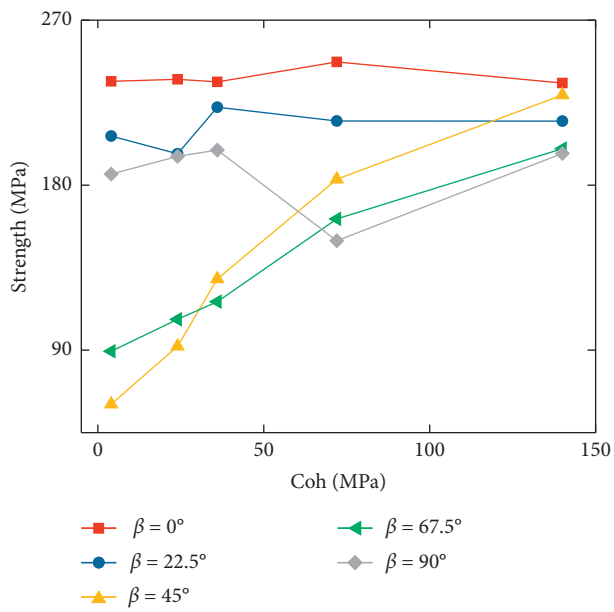

(g)

Figure 9: The cumulative distribution curve and average fragment size of layered rocks with different bedding shear strength. (a–e) The distribution curve of 0°, 22.5°, 45°, 67.5°, and 90° samples, red: coh = 4 MPa, blue: coh = 24 MPa, yellow: coh = 36 MPa, green: coh = 72 MPa, and gray: coh = 140 MPa. (f) Average fragment size vs. bedding shear strength under different bedding angles. (g) Dynamic strength vs. bedding shear strength under different bedding angles.

direction and the bedding dip angle should be changed under different impact forces.

4.2. Effect of Weak Bedding Strength

4.2.1. Effect of Weak Bedding Shear Strength. The weak bedding plane is endowed with cohesion strength for 4 MPa, 24 MPa, 36 Mpa, 72 Mpa, and 140 MPa, respectively, as shown in Figure 9. The minimum strength corresponds to the weak bedding immediately destroyed; the last is the bond strength of matrix.

Tien et al. [32] studied the properties of homogeneous rock-like materials and layered materials under static loading. It is considered that the failure of $\beta = 0^\circ$ samples is not affected by the bedding as the compressive strength is similar to that of isotropic rock. However, from the view of rock failure, it was found that the bedding would disturb the crack propagation of the specimen. When the shear strength of the bedding plane is minor, the bedding as a weak plane leads to the local fracture of 0°–22.5° specimen. And there is no preferential defect in the sample as the shear strength increases, so the degree of fragmentation decreases.

The situation becomes complicated for 45° specimens. The bedding plane was destroyed first at low bedding shear strength, and the failure that was perpendicular to the weak plane of bedding has happened, which leads to the further fracture of the specimen. However, in the case of high bedding shear strength, the bedding no longer hinders the propagation of the splitting crack, resulting in smaller fragments of the specimen. At the same time, the bedding shear strength makes no contribution to the crack growth and dynamic strength of the 90° samples.

4.2.2. Effect of Weak Bedding Tension Strength. At each bedding angle, five kinds of tensile strength weak plane specimens are loaded, from the weakest 0.01 MPa to 52 MPa as same as with the matrix. The results listed in Figure 10 illustrate that the tensile strength of the weak plane has little effect on the ultimate fragment state and the dynamic compression strength. In most cases, the upper part of the cumulative curve causes differentiation, pointing that the tensile strength mainly limits the generation of large pieces.

Only for 0° specimen, the crack was harder to develop as the strength enhanced. Compared with the bedding shear strength situation, it could be seen that the bedding shear strength influences the failure of 22.5° specimen, while the 0° specimen is mainly damaged by tensile strength at strain rate≈120 s^{-1}. The average size of high bedding angle specimen is kept at a small level and near-zero strength results in less fragmentation.

4.3. Effect of Weak Bedding Stiffness. The initial kn/ks of bedding is 2.46, which is changed to explore the influence of stiffness on rock fragmentation, as shown in Figure 11. It is obvious that the bedding stiffness has no effect on the failure of layered rock. However, the average fragment size of high angle samples tends to be consistent when the kn gradually increase. The failure of bedding plane occurs in the initial loading stage, which results in its ability to resist

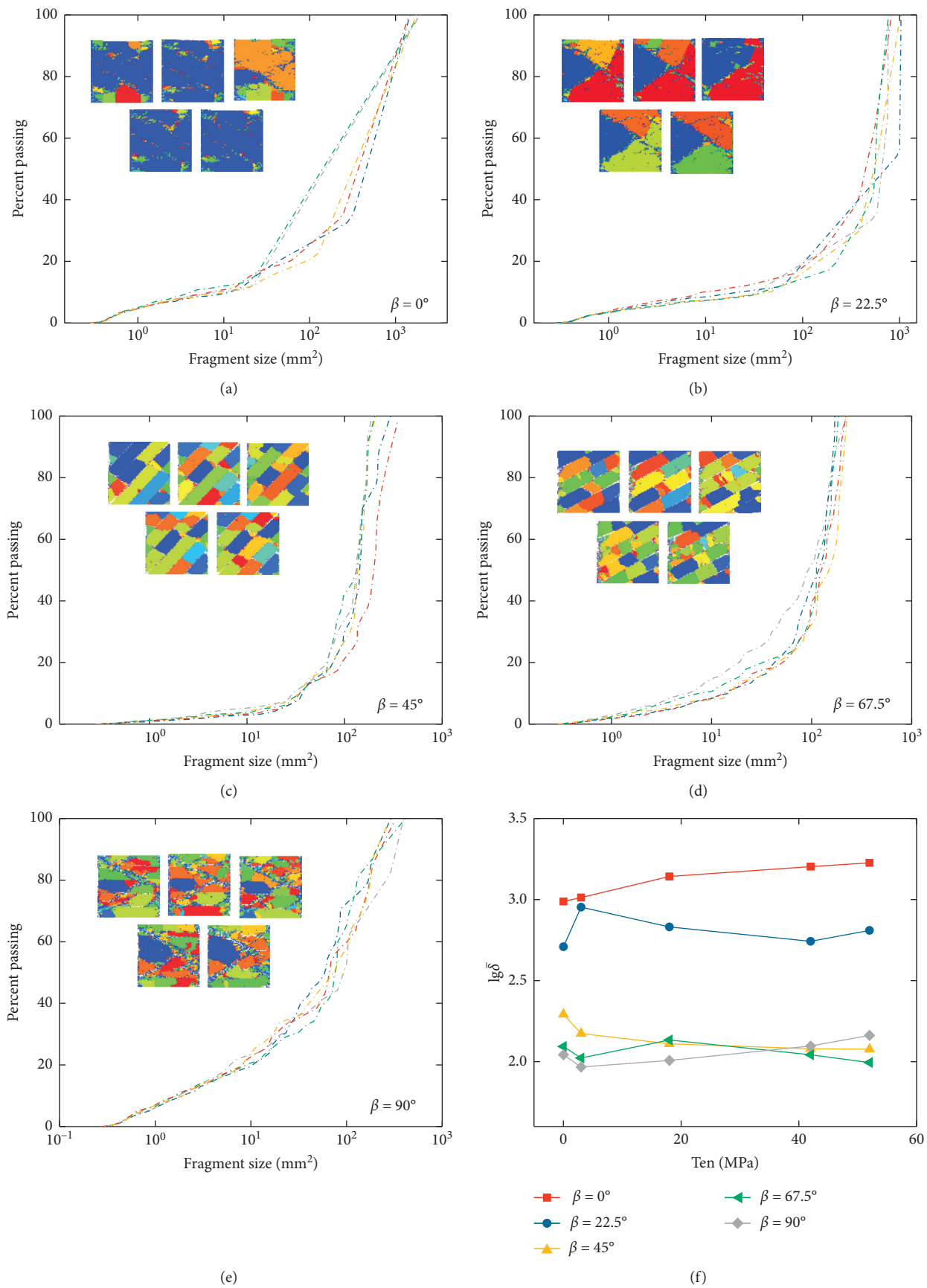

Figure 10: Continued.

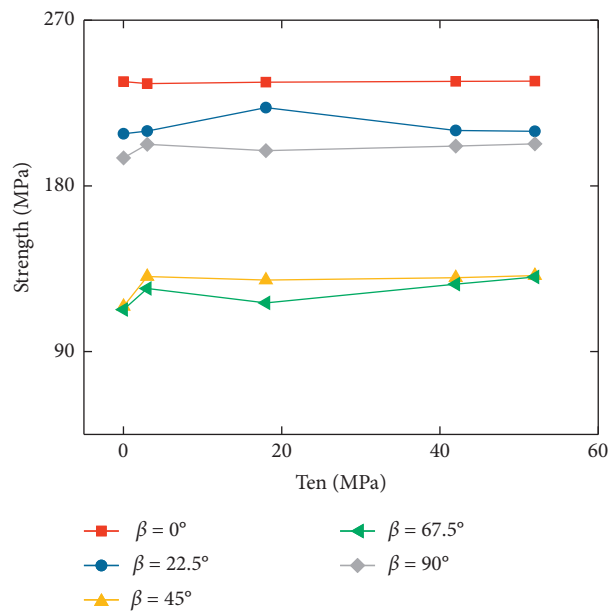

(g)

Figure 10: The cumulative distribution curve and average fragment size of layered rocks with different bedding tensile strength. (a–e) The distribution curve of 0°, 22.5°, 45°, 67.5°, and 90° samples, red: ten = 0.01 MPa, blue: ten = 3 MPa, yellow: ten = 18 MPa, green: ten = 42 MPa, and gray: ten = 52 MPa. (f) Average fragment size vs. bedding tension strength under different bedding angles. (g) Dynamic strength vs. bedding tension strength under different bedding angles.

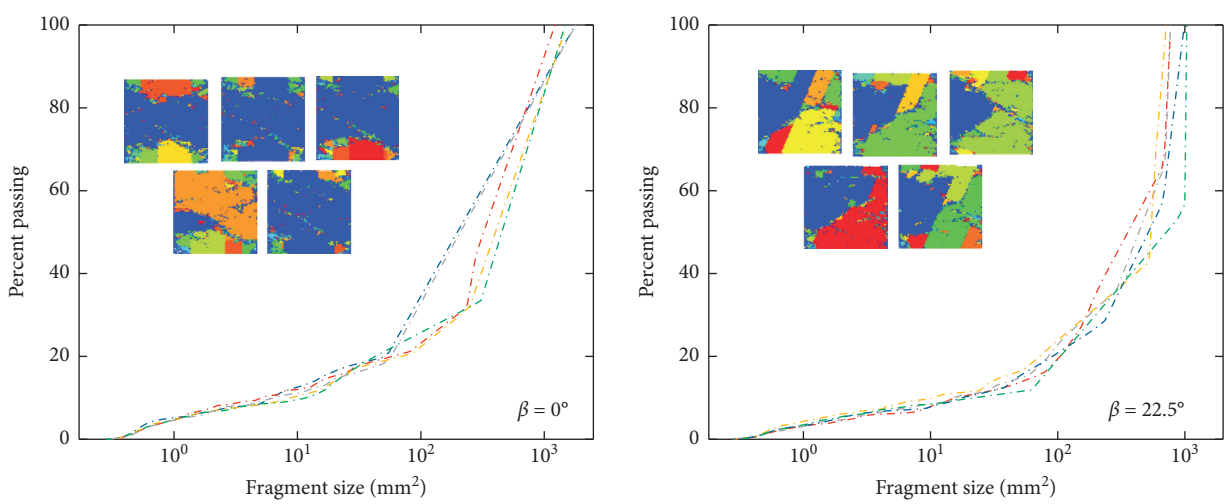

(a) (b)

Figure 11: Continued.

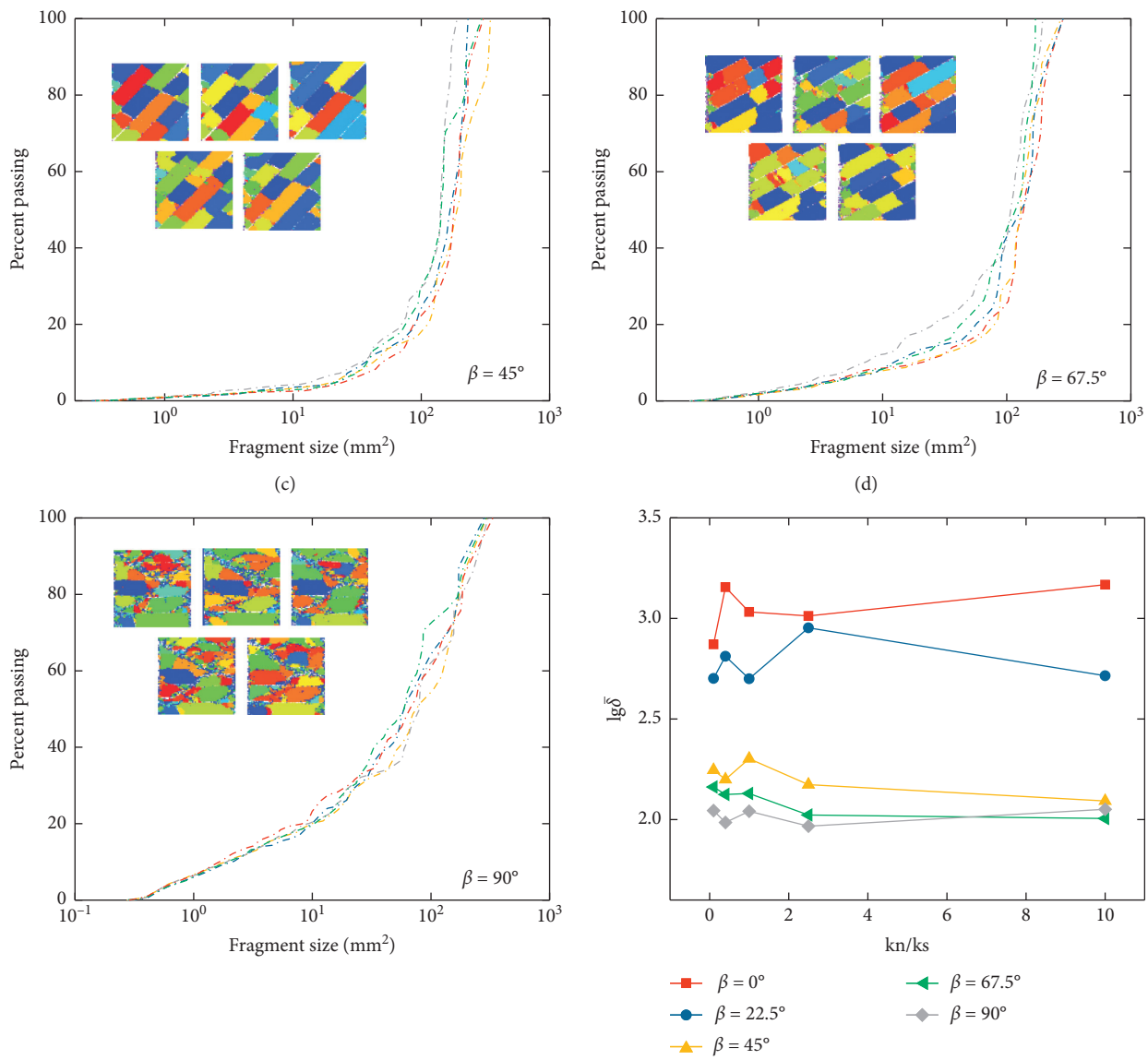

Figure 11: Continued.

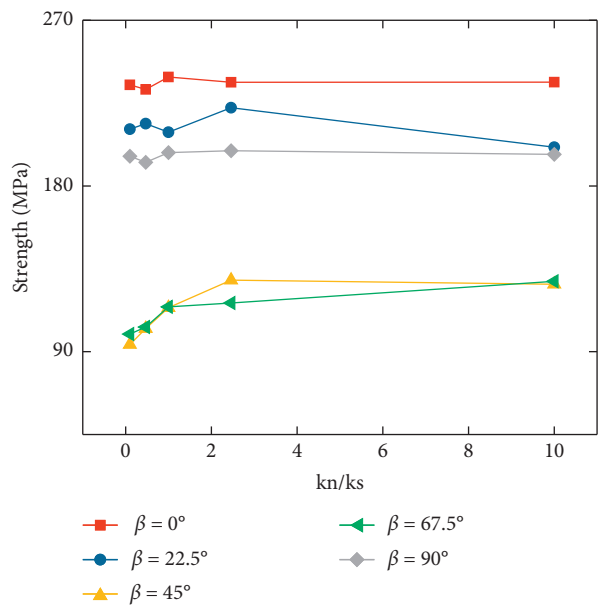

(g)

Figure 11: The cumulative distribution curve and average fragment size of layered rocks with different bedding stiffness. (a–e) The distribution curve of 0°, 22.5°, 45°, 67.5°, and 90° samples, red: ks/kn = 10, blue: ks/kn = 2.46, yellow: kn/ks = 1, green: kn/ks = 2.46, and gray: kn/ks = 10. (f) Average fragment size vs. bedding stiffness under different bedding angles. (g) Dynamic strength vs. bedding stiffness under different bedding angles.

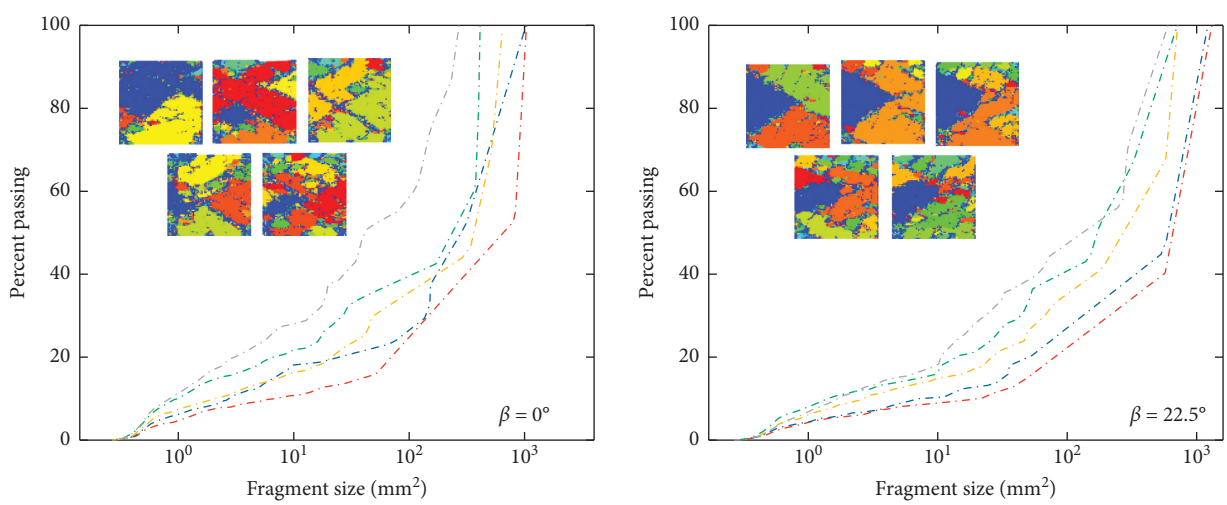

(a) (b)

Figure 12: Continued.

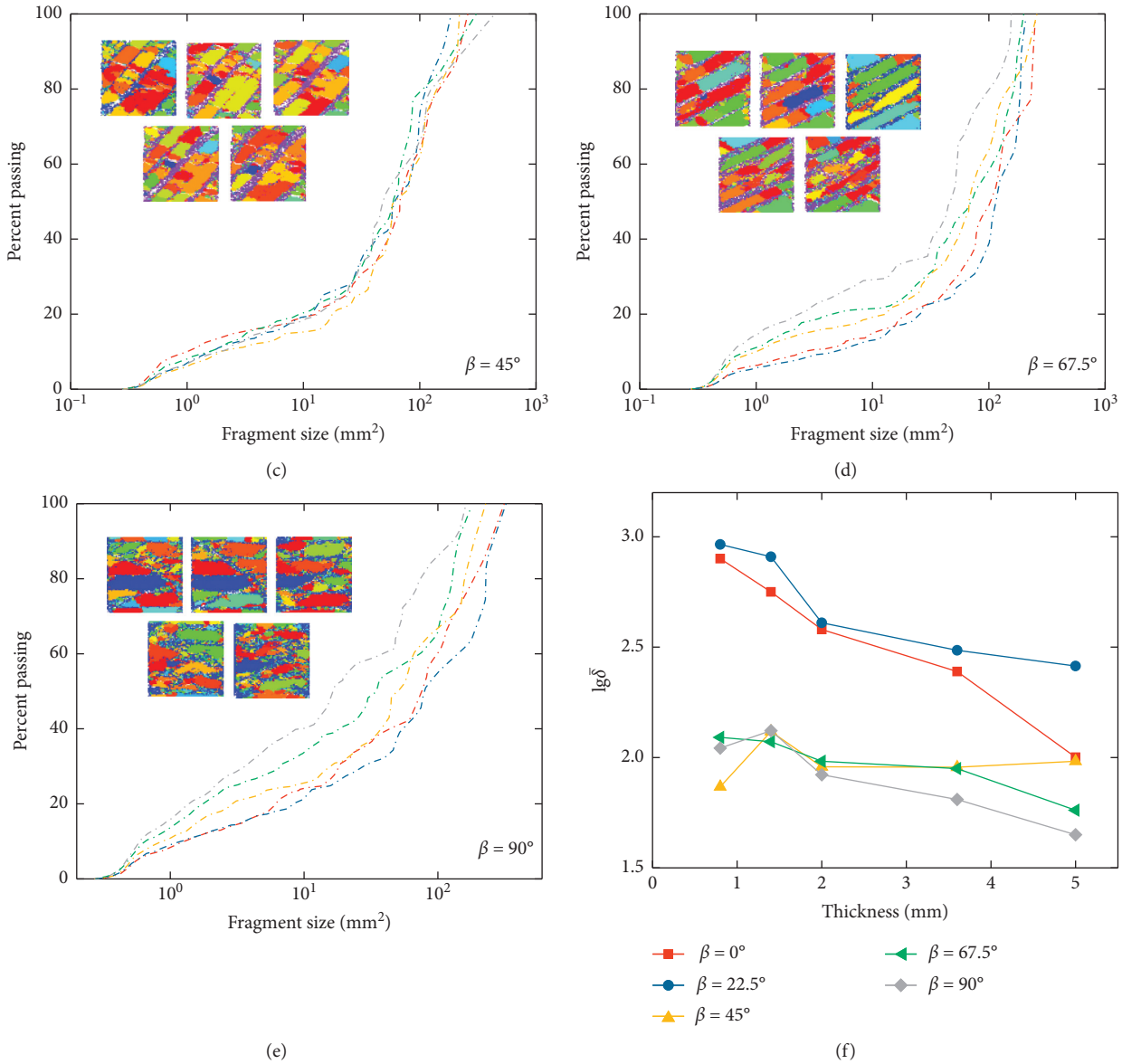

Figure 12: Continued.

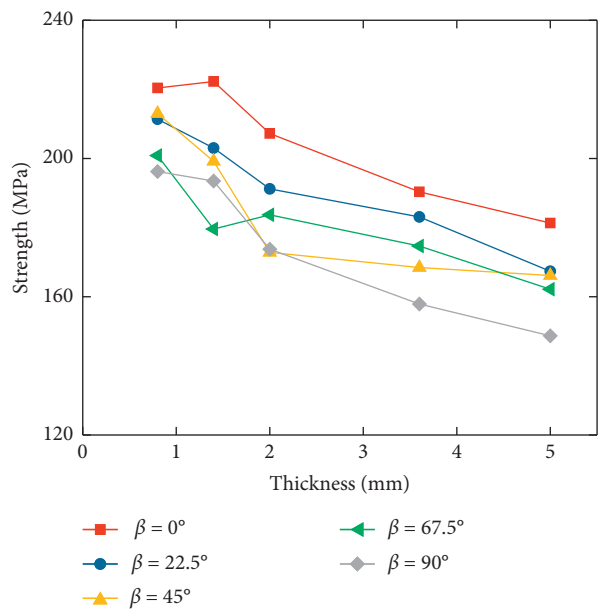

(g)

Figure 12: The cumulative distribution curve and average fragment size of layered rocks with different bedding thickness. (a–e) The distribution curve of 0°, 22.5°, 45°, 67.5°, and 90° samples, red: thickness = 0.8 mm, blue: thickness = 1.4 mm, yellow: thickness = 2.0 mm, green: thickness = 3.6 mm, and gray: thickness = 5.0 mm. (f) Average fragment size vs. thickness under different bedding angles. (g) Dynamic strength vs. thickness under different bedding angles.

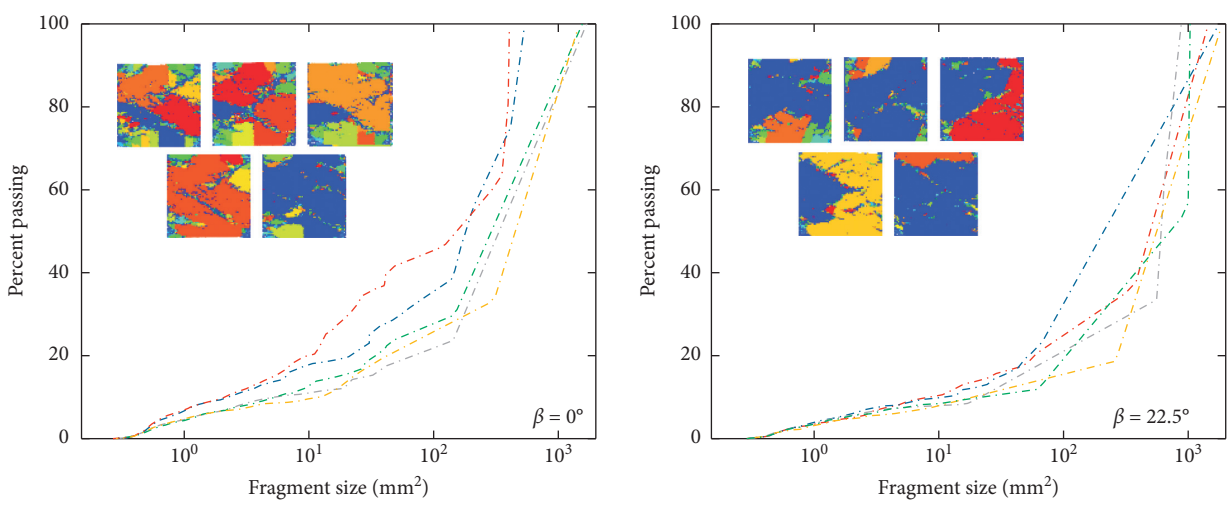

(a) (b)

Figure 13: Continued.

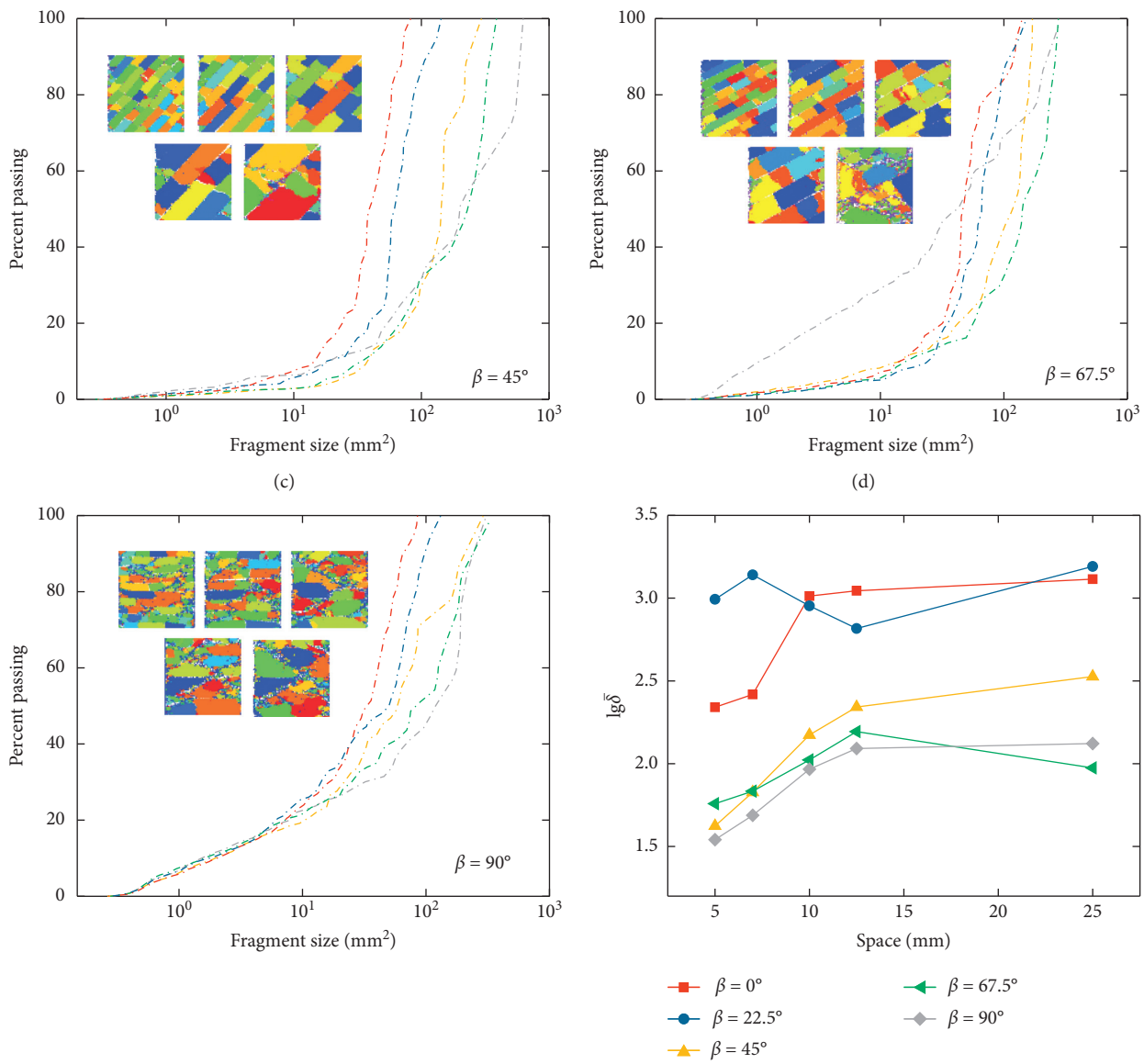

Figure 13: Continued.

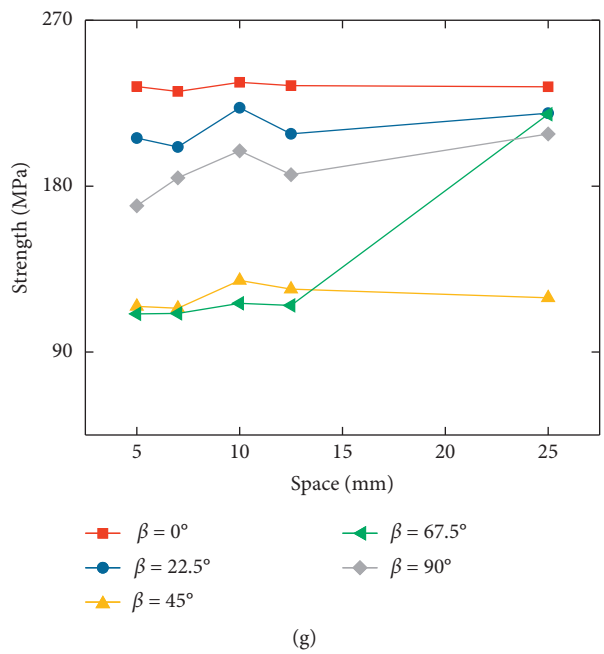

Figure 13: The cumulative distribution curve and average fragment size of layered rocks with different bedding space. (a–e) The distribution curve of 0°, 22.5°, 45°, 67.5°, and 90° samples, red: space = 5 mm, blue: space = 6.5 mm, yellow: space = 10 mm, green: space = 12.5 mm, and gray: space = 25 mm. (f) Average fragment size vs. bedding space under different bedding angles. (g) Dynamic strength vs. bedding space under different bedding angles.

deformation having no longer an effect on the crack propagation.

4.4. Effect of Weak Bedding Thickness. As shown in Figure 12, weak plane models with thicknesses of 0.8 mm, 1.4 mm, 2.0 mm, 3.6 mm, and 5.0 mm are constructed. The bedding strength is half of the original matrix, rather than using SJ model to avoid the distortion of the simulation results led by all the SJ model damage during loading. The smallest thickness represents the existence of a weak surface. In the case of 5.0 mm, half sample is strong matrix and the other is weak. It could be seen from Figure 12 that when there exist weak planes in the 45° specimen, the central bedding plane divides the specimen into two parts, bearing the load separately. As a result, the bearing capacity of the 45° specimens changed little under different conditions, which lead to similar failure patterns for 45° specimens.

However, the bearing capacity and failure mode of specimens with other bedding angles change greatly when the proportion of weak plane increases. The simulation reveals that more defects lead to greater fragmentation and the size has a significant downward trend for all angles except 45°, which means most angle rocks are sensitive to it. At the same time, the distribution curves for 45° specimen have little differences and others move left as a whole. The weak plane always makes the specimen with high angle easier to develop more cracks regardless of its width, compared to 22.5° specimen being the most difficult to be further damaged.

4.5. Effect of Weak Bedding Space. A smaller spacing means that the number of laminations increases, which changes from 10 to 1. It could be analyzed from Figure 13 that when the bedding angle is greater than 45°, the failure of the specimens under any spacing is influenced by the bedding plane. And more split cracks begin to appear due to the barrier effect of weak plane being weakened when there is only one weak plane. The smaller fragment would emerge as the split crack intersects with the weak plane. The local failure of specimens is controlled by the bedding planes when the spacing is less than 12 mm for the specimens with low bedding angle. However, the effect of bedding planes for 0° specimens is no longer significant with the space increasing, while that of 22.5 specimens still affects local fracture. As a result, the fragment distribution of other bedding dip angle samples except 22.5° correspondingly shifts to the left when the bedding space decreases. Nevertheless, the average fragment size rises slightly when the space exceeds a quarter.

5. Conclusions

The effect of the microscopic properties of bedding and strain rate on the fragment size distributions of layered rock with different bedding dip angles was investigated by using the 2D discrete element model. Several conclusions were drawn from the experiment:

(1) A SHPB numerical model was established and validated. A new method to obtain reasonable layered rock

dynamic simulation result is proposed. The quasistatic and dynamic test results are combined to calibrate the elastic modulus and strength of layered rock to reproduce the stress–strain curve and ultimate fragment state.

(2) The average size of samples with different bedding angles decreases as the strain rate increases, while the strength presents an opposite trend. The samples tend to become pulverized under high strain rate, especially for the low bedding angle samples as more cracks initiate along the loading direction and propagate to intersect with the cracks.

(3) It is harder for the samples with low dip angle to be damaged if the bedding shear strength is added, while the fragmentation of high angle samples does not change significantly. The average fragment size of 45° samples varies greatly with the shear strength because the failure mode of the specimens changed. And the failure of layered specimens with all dip angles is not affected by the tensile strength and stiffness.

(4) The wider bedding may promote the crack initiation and propagation under the same impact load, which means large fragments develop into small ones. It was initially considered that the effect of bedding plane on low dip angle samples is not considerable. However, the bedding has a dramatic impact on the final fragment.

(5) Because the effect of hindering splitting crack has always existed for the bedding plane of 22.5° sample and more cracks initiate along the loading direction, the fragment size distribution curve of all bedding angle samples gradually moves to the right when the bedding space increases except for the 22.5° samples. Nevertheless, the average fragment size rises slightly when the space exceeds a range.

Data Availability

Some data, models, or codes generated or used during the study are available from the corresponding author upon request: static mechanical properties of layered phyllite with different bedding angles and all results of the dynamic compression test.

Conflicts of Interest

The authors declare that they have no conflicts of interest regarding the publication of this paper.

Acknowledgments

The constructive comments of three anonymous reviewers are appreciated. This work received funding from the National Natural Science Foundation of China (Nos. 51439008 and 51679231) and China Scholarship Council (to the first author, No. 202004910629).

References

[1] C. V. B. Cunningham, "Fragmentation estimations and the Kuz-Ram model–four years on," in *Proceedings of the 2nd International Symposium on Rock Fragmentation by Blasting*, pp. 475–487, Keystone, CO, USA, August 1987.

[2] X. F. Li, H. B. Li, Y. Q. Liu, Q. C. Zhou, and X. Xia, "Numerical simulation of rock fragmentation mechanisms subject to wedge penetration for TBMs," *Tunnelling and Underground Space Technology*, vol. 53, pp. 96–108, 2016.

[3] J. C. Li, H. B. Li, and J. Zhao, "An improved equivalent viscoelastic medium method for wave propagation across layered rock masses," *International Journal of Rock Mechanics and Mining Sciences*, vol. 73, no. 1, pp. 62–69, 2015.

[4] F. Gong, W. Wuxing Wu, T. Tianbin Li, and X. Xuefeng Si, "Experimental simulation and investigation of spalling failure of rectangular tunnel under different three-dimensional stress states," *International Journal of Rock Mechanics and Mining Sciences*, vol. 122, p. 104081, 2019.

[5] D. A. Shockey, D. R. Curran, L. Seaman, J. T. Rosenberg, and C. F. Petersen, "Fragmentation of rock under dynamic loads," *International Journal of Rock Mechanics and Mining Sciences & Geomechanics Abstracts*, vol. 11, no. 8, pp. 303–317, 1974.

[6] F. Q. Gong, S. Luo, G. Lin, and X. B. Li, "Evaluation of shear strength parameters of rocks by preset angle shear, direct shear and triaxial compression tests," *Rock Mechanics and Rock Engineering*, vol. 53, no. 5, pp. 2505–2519, 2020.

[7] X. F. Li, H. B. Li, Q. B. Zhang, J. L. Jiang, and J. Zhao, "Dynamic fragmentation of rock material: characte-ristic size, fragment distribution and pulverization law," *Engineering Fracture Mechanics*, vol. 199, pp. 739–759, 2018.

[8] J. D. Hogan, R. J. Rogers, J. G. Spray, and S. Boonsue, "Dynamic fragmentation of granite for impact energies of 6–28 J," *Engineering Fracture Mechanics*, vol. 79, pp. 103–125, 2012.

[9] P. Rosin and E. Rammler, "The laws governing the fineness of powdered coal," *Journal of Institute of Fuel*, vol. 7, pp. 29–36, 1933.

[10] N. F. Mott and E. H. Linfoot, "Ministry of supply, The raw material guide," *The Analyst*, vol. 68, no. 806, 1943.

[11] D. E. Grady, "Local inertial effects in dynamic fragmentation," *Journal of Applied Physics*, vol. 53, no. 1, pp. 322–325, 1982.

[12] F. Zhou and J. F. Molinari, "On the rate-dependency of dynamic tensile strength of a model ceramic system," *Computer Methods in Applied Mechanics and Engineering*, vol. 194, no. 12-16, pp. 1693–1709, 2005.

[13] X. F. Li, X. Li, H. B. Li, Q. B. Zhang, and J. Zhao, "Dynamic tensile behaviours of heterogeneous rocks: the grain scale fracturing characteristics on strength and fragmentation," *International Journal of Impact Engineering*, vol. 118, pp. 98–118, 2018.

[14] F. Q. Gong, X. B. Li, and X. L. Liu, "Preliminary experimental study of characteristics of rock subjected to 3D coupled static and dynamic loads," *Chinese Journal of Rock Mechanics and Engineering*, vol. 30, no. 6, pp. 1179–1190, 2011.

[15] S. Levy and J. F. Molinari, "Dynamic fragmentation of ceramics, signature of defects and scaling of fragment sizes," *Journal of the Mechanics and Physics of Solids*, vol. 58, no. 1, pp. 12–26, 2010.

[16] B. Paliwal and K. T. Ramesh, "An interacting micro-crack damage model for failure of brittle materials under compression," *Journal of the Mechanics and Physics of Solids*, vol. 56, no. 3, pp. 896–923, 2008.

[17] R. J. Wu, H. B. Li, X. F. Li, X. Xia, and L. W. Liu, "Experimental study and numerical simulation of the dynamic behavior of transversely isotropic phyllite," *International Journal of Geomechanics*, vol. 20, no. 8, Article ID 04020105, 2020.

[18] X. Ou, X. Zhang, H. Feng, C. Zhang, and J. Yang, "Effect of the confining pressure on the dynamic compression properties of

transversely isotropic rocks," *Advances in Civil Engineering*, vol. 6, p. 11, 2019.

[19] H.-B. Du, F. Dai, Y. Xu, Y. Liu, and H.-n. Xu, "Numerical investigation on the dynamic strength and failure behavior of rocks under hydrostatic confinement in SHPB testing," *International Journal of Rock Mechanics and Mining Sciences*, vol. 108, pp. 43–57, 2018.

[20] X. F. Li, Q. B. Zhang, H. B. Li, and J. Zhao, "Grain-based discrete element method (GB-DEM) modelling of multi-scale fracturing in rocks under dynamic loading," *Rock Mechanics and Rock Engineering*, vol. 51, no. 12, pp. 3785–3817, 2018.

[21] F. Dai, M. D. Wei, N. W. Xu, Y. Ma, and D. S. Yang, "Numerical assessment of the progressive rock fracture mechanism of cracked chevron notched Brazilian disc specimens," *Rock Mechanics and Rock Engineering*, vol. 48, no. 2, pp. 463–479, 2015.

[22] B. Park and K.-B. Min, "Bonded-particle discrete element modeling of mechanical behavior of transversely isotropic rock," *International Journal of Rock Mechanics and Mining Sciences*, vol. 76, pp. 243–255, 2015.

[23] E. Cadoni, "Dynamic characterization of orthogneiss rock subjected to intermediate and high strain rates in tension," *Rock Mechanics and Rock Engineering*, vol. 43, no. 6, pp. 667–676, 2010.

[24] Y. X. Zhou, K. Xia, X. B. Li et al., "Suggested methods for determining the dynamic strength parameters and Mode-I fracture toughness of rock materials," *International Journal of Rock Mechanics and Mining Sciences*, vol. 49, no. 1, pp. 105–112, 2011.

[25] F. Dai, K. Xia, J. P. Zuo, R. Zhang, and N. W. Xu, "Static and dynamic flexural strength anisotropy of Barre granite," *Rock Mechanics and Rock Engineering*, vol. 46, no. 6, pp. 1589–1602, 2013.

[26] F.-Q. Gong, X.-F. Si, X.-B. Li, and S.-Y. Wang, "Dynamic triaxial compression tests on sandstone at high strain rates and low confining pressures with split Hopkinson pressure bar," *International Journal of Rock Mechanics and Mining Sciences*, vol. 113, pp. 211–219, 2019.

[27] X. F. Li, H. B. Li, L. W. Liu et al., "Investigating the crack initiation and propagation mechanism in brittle rocks using grain-based finite-discrete element method," *International Journal of Rock Mechanics and Mining Sciences*, vol. 127, p. 104219, 2020.

[28] F. Gong and J. Hu, "Energy dissipation characteristic of red sandstone in the dynamic Brazilian disc test with SHPB setup," *Advances in Civil Engineering*, vol. 2020, Article ID 7160937, 10 pages, 2020.

[29] J. C. Li, H. B. Li, G. W. Ma, and J. Zhao, "A time-domain recursive method to analyse transient wave propagation across rock joints," *Geophysical Journal International*, vol. 188, no. 2, pp. 631–644, 2012.

[30] P. A. Cundall, "A computer model for simulating progressive, large-scale movement in blocky rock system," in *Proceedings of the International Symposium on Rock Mechanics*, Nancy, France, October 1971.

[31] B. Park, K.-B. Min, N. Thompson, and P. Horsrud, "Three-dimensional bonded-particle discrete element modeling of mechanical behavior of transversely isotropic rock," *International Journal of Rock Mechanics and Mining Sciences*, vol. 110, pp. 120–132, 2018.

[32] Y. M. Tien, M. C. Kuo, and C. H. Juang, "An experimental investigation of the failure mechanism of simulated transversely isotropic rocks," *International Journal of Rock Mechanics and Mining Sciences*, vol. 43, no. 8, pp. 1163–1181, 2006.